










Formation of two-ion crystals by injection from a Paul-trap source into a high-magnetic-field Penning trap

J. Berrocal ¹, E. Altozano ¹, F. Domínguez ¹, M. J. Gutiérrez ^{1,*}, J. Cerrillo ², F. J. Fernández ³, M. Block ^{4,5,6},
C. Ospelkaus ^{7,8} and D. Rodríguez ^{1,9,†}

¹*Departamento de Física Atómica, Molecular y Nuclear, Universidad de Granada, 18071 Granada, Spain*

²*Área de Física Aplicada, Universidad Politécnica de Cartagena, 30202 Cartagena, Spain*

³*Departamento de Arquitectura y Tecnología de Computadores, Universidad de Granada, 18071 Granada, Spain*

⁴*Department Chemie - Standort TRIGA, Johannes Gutenberg-Universität Mainz, D-55099 Mainz, Germany*

⁵*GSI Helmholtzzentrum für Schwerionenforschung GmbH, D-64291 Darmstadt, Germany*

⁶*Helmholtz-Institut Mainz, D-55099 Mainz, Germany*

⁷*Institute of Quantum Optics, Leibniz Universität Hannover, Welfengarten 1, 30167 Hannover, Germany*

⁸*Physikalisch-Technische Bundesanstalt, Bundesallee 100, 38116 Braunschweig, Germany*

⁹*Centro de Investigación en Tecnologías de la Información y las Comunicaciones, Universidad de Granada, 18071 Granada, Spain*



(Received 20 November 2021; revised 25 March 2022; accepted 3 May 2022; published 16 May 2022)

Two-ion crystals constitute a platform for investigations of quantum nature that can be extended to any ion species or charged particle provided one of the ions in the crystal can be directly laser cooled and manipulated with laser radiation. This paper presents the formation of two-ion crystals for quantum metrology in a 7-tesla open-ring Penning trap. $^{40}\text{Ca}^+$ ions are produced either internally by photoionization or externally in a (Paul-trap) source, transported through the strong magnetic field gradient of the superconducting solenoid, and captured in-flight with a mean kinetic energy of a few electronvolts with respect to the minimum of the Penning-trap potential well. Laser cooling of the two-ion crystal in a strong magnetic field towards reaching the quantum regime is also presented, with particular emphasis on the cooling of the radial modes.

DOI: [10.1103/PhysRevA.105.052603](https://doi.org/10.1103/PhysRevA.105.052603)

I. INTRODUCTION

The precise control of individual (or a pair of) charged particles, or particle-antiparticle pairs in Penning traps, is a prerequisite to perform accurate measurements of the eigenfrequencies of the stored particle and/or antiparticle [1–4] with implications in tests of fundamental symmetries (see, e.g., Ref. [5] for a recent review). The control of the charged particle down to the lowest motional energy in a Penning trap, only possible by performing laser cooling [6,7], moves the experiments on precise motional frequency measurements to a new regime of quantum nature [8]. However, in most cases, the cooling of the charged particle under study relies on the Coulomb interaction between the particle and an auxiliary ion that can be laser cooled [9]. The ion (sensor) and the charged particle to be studied may be stored in physically separated Penning traps [10–13], in different potential wells [14], or in the same one [8,15]. The sensor shall provide the information of the system as the target is blind to laser radiation. If such a platform can be coupled to an external ion source, it can turn into a universal atomic or molecular mass spectrometer. This is crucial for the production of any target ion as well as the sensor species in a well-controlled manner, outside

the Penning trap. For example, the formation of antimatter particles or exotic radionuclides is usually accomplished in nuclear reactions resulting in few particles at high energy and with large momentum spread, so that an additional preparation stage is mandatory [16–18]. Furthermore, the production of the sensor ion outside the Penning trap will avoid charge exchange between the laser-cooled sensor ion/s and hotter (sensor) atoms [19] to the advantage of experiments where the coolant source has to be in continuous operation. The injection of ions produced outside a Penning trap is well known in experiments devoted to precision mass spectrometry, where the target ion is probed without laser cooling (see, e.g., extreme scenarios described in Refs. [20,21]). This is not the case in laser cooling Penning-trap experiments (and, in general, in similar experiments with other kinds of ion traps) devoted to quantum sensing or quantum information processing [7,22,23]. In those experiments, the ion species to be laser cooled are generally produced inside the Penning trap either by laser desorption on a metallic sample located close to the trap electrodes (see, e.g., [24]) or by photoionization or electron impact ionization of atoms released from an oven, as initially done in the experiments reported here. Thus, the combination of external ion production and in-trap laser cooling has not been much exploited. Results from only a few experiments have been reported. In Ref. [25], Be^+ ions were produced by laser ablation upstream from a Penning trap, where they were injected, laser cooled, and utilized for sympathetic cooling of positrons. Ion crystals in a Penning

*Present address: GSI Helmholtzzentrum für Schwerionenforschung GmbH, D-64291 Darmstadt, Germany.

†danielrodriguez@ugr.es

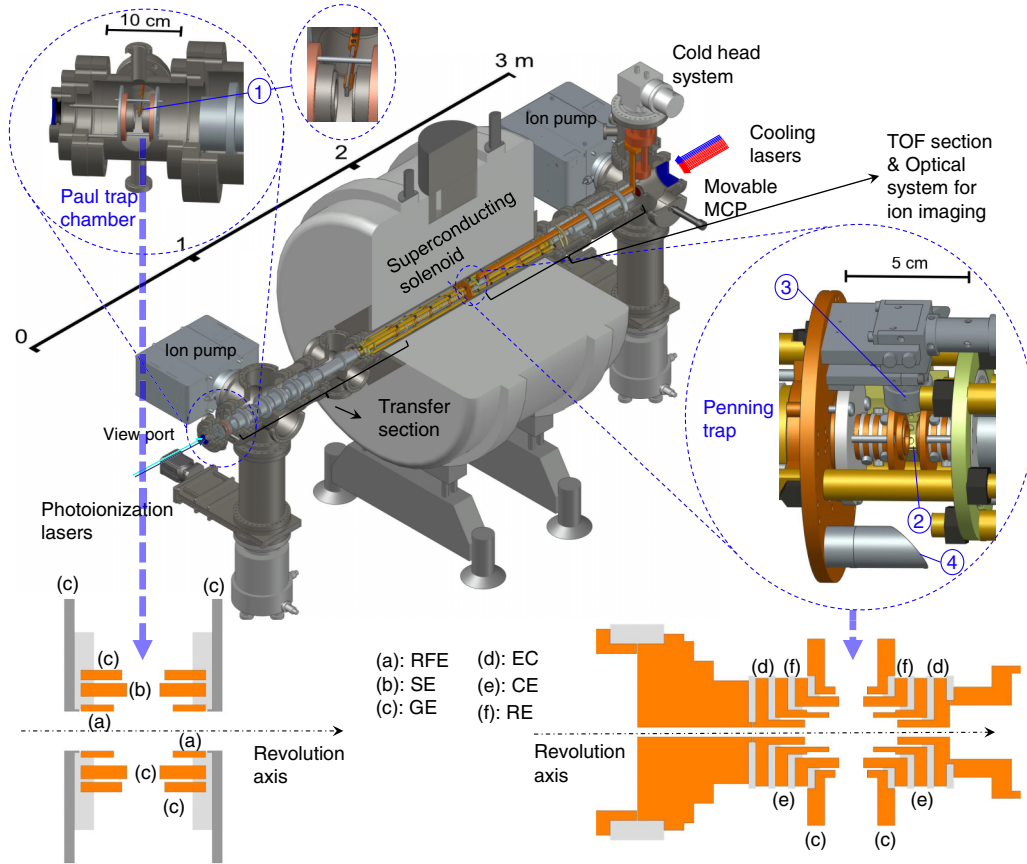


FIG. 1. Three-dimensional CAD drawing of the Penning-traps beam line. The most important elements are indicated. The open-ring traps (Paul and Penning) are zoomed. Number 1 indicates an atomic oven in the Paul-trap chamber; number 2 points out the MACOR[®] Machinable Glass Ceramic structure surrounding the atomic oven oriented to the center of the open-ring Penning trap. Number 3 indicates the housing of the optical objective to collimate the fluorescence photons and number 4 points at the support structure of one of the mirrors to direct the cooling laser beams in the radial plane of the ions’ motion. Longitudinal cuts of the Paul and Penning trap are shown, indicating the different electrodes in orange (insulators are in gray). RFE: radio-frequency electrode(s); SE: switching electrode; GE: all the electrodes at ground. The nomenclature for the Penning-trap electrodes is as in Ref. [26]: EC, CE, and RE are the endcap(s), correction(s), and ring(s) electrodes, respectively. More details are given in the text.

trap from externally produced $^{24}\text{Mg}^+$ ions have been formed at GSI-Darmstadt in the SpecTrap experiment [27], aiming at creating a bath of coolant ions for sympathetic cooling of highly charged ions, to perform laser spectroscopy experiments on the latter. In that work, only axial cooling was applied and crystals formed with many ions were reported showing different planes in the radial direction, but never a few-ion crystal oriented in the direction of the magnetic field. Other experiments using externally produced target ions are those on quantum-logic spectroscopy on highly charged ions at PTB-Braunschweig [28] or to perform studies on $^{232}\text{Th}^+$ at the University of Mainz [29]. Both use radio-frequency traps and still work with the internal ion production of the coolant-and-sensor ion.

In this paper, we report on the formation of ion crystals in an open-ring Penning trap [26], when the ions are produced by photoionization in a Paul trap made of concentric rings [30,31]. This trap is located in the beam line outside the superconducting solenoid providing the largest magnetic field used for a Penning-trap laser-cooling experiment [26]. The injection can be controlled down to just one ion by means of evaporative cooling by lowering down the trap voltages.

In addition, the geometry of the Paul trap with an open diameter of 10 mm allows through-transport of any ion species produced by other sources upstream, which can also be relevant for accelerator-based experiments. The production of a single laser-cooled ion and a balanced two-ion crystal in a 7-tesla magnetic field is demonstrated and characterized. The two mechanisms utilized to cool the magnetron motion and motional modes in both systems have been studied and the advantage of having a high magnetic field strength is presented. In the Appendix, we show Coulomb crystals with a large number of ions produced with this setup, which we use to obtain an upper limit of the ions’ temperature. Coulomb crystals have previously been extensively studied by several groups (see, e.g., [32,33]).

II. EXPERIMENTAL SETUP

The Penning-traps beam line at the University of Granada is shown in Fig. 1. It has been modified from that described in Ref. [26] by introducing a Paul trap [30] in the transfer section. The superconducting solenoid provides, in the room-temperature bore, two highly homogeneous magnetic field

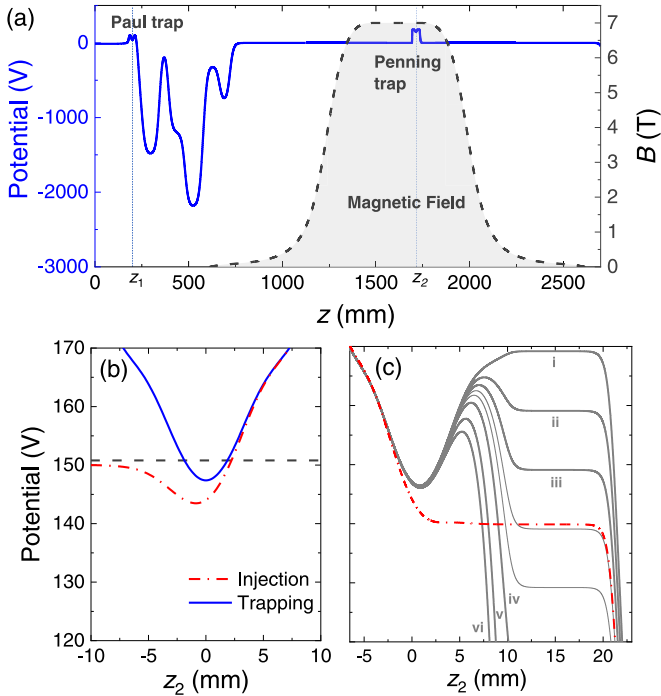


FIG. 2. (a) Electric potentials and magnetic field strength along the Penning-traps beam line. The electrostatic potential is given on the left axis, while the magnetic field strength (dashed line surrounding the gray-shaded area) is given on the right one. $z_1 = z - 200$ mm and $z_2 = z - 1733$ mm. (b) The dc potential in the open-ring Penning trap for injection and trapping, and (c) potential shapes for adiabatic and energy-selective extraction of the ions from the Penning trap (not all the potentials used in the experiment are shown); (i) $V_{EC} = 170$ V, (ii) $V_{EC} = 160$ V, (iii) $V_{EC} = 150$ V, (iv) $V_{EC} = 110$ V, (v) $V_{EC} = 50$ V, and (vi) $V_{EC} = -20$ V. $V_{CE} = 168$ V and $V_{RE} = 150$ V. The horizontal dashed line in (b) represents the mean ions' kinetic energy. The dash-dotted red line in (c) is a potential configuration to extract all the ions from the trap. The dc potentials are extracted from SIMION simulations [34].

regions in a volume of 1 cm^3 each, separated by 20 cm. The center of the first of these regions ($\Delta B/B \sim 10$ ppm) coincides with the center of a preparation Penning trap made of a stack of cylinders [35], which is grounded in the experiments described here and foreseen for further preparation of other ion species. The second highly homogeneous region ($\Delta B/B \sim 0.1$ ppm) coincides with the center of the open-ring Penning trap displayed in Fig. 1 [26], where the experiments on the two-ion crystal are carried out. The trap tower is housed in a customized tube inside the magnet bore. Two turbomolecular pumps, one at each side of the magnet, with a pumping speed of 800 l/s (for N_2) each, and two ion pumps, clearly visible in the figure with pumping speeds of 300 l/s and 600 l/s at the transfer and time-of-flight (TOF) sections, respectively, provide a vacuum at the pump side of the order of 10^{-10} mbar, which allows one to reach about 10^{-9} mbar in the trap volume. This is possible by means of a copper bar which ends close to the trapping region and is connected on the other side to the first stage of a cold-head system at 40 K. The two traps are zoomed in Fig. 1, where also the longitudinal cuts with the different electrodes are shown.

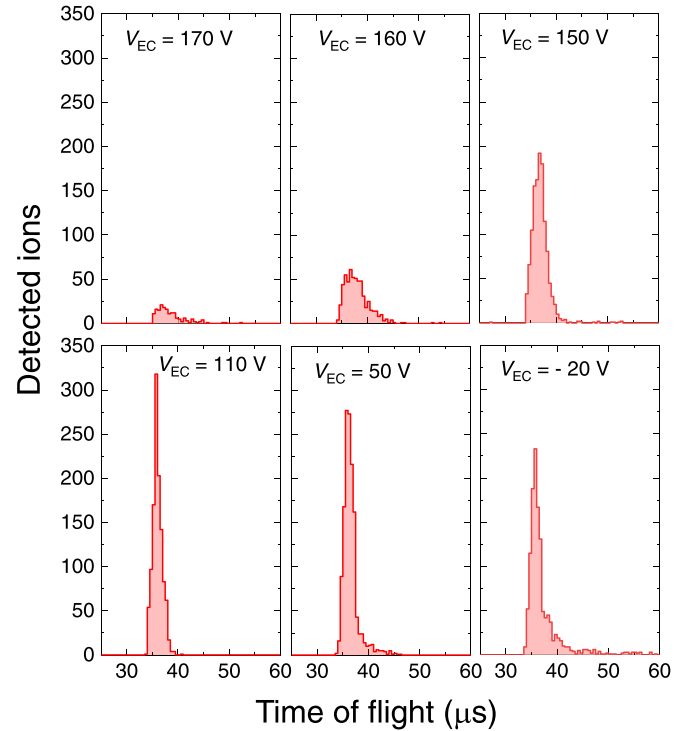


FIG. 3. Time-of-flight signal of ions from the open-ring Penning trap to the MCP detector for several values of V_{EC} . 1000 cycles have been accumulated. The ions are produced by photoionization in the Paul trap during one second, ejected, transferred, and captured in the Penning trap, held for 20 ms, and ejected again towards the MCP detector at the end of the beam line. Different potentials have been applied for extraction. These potentials are depicted in Fig. 2(c), from (i) to (vi). The ions are not cooled for these measurements.

The production of ions is done by photoionization of calcium atoms, using two laser beams with wavelengths around 423 nm (tunable) and 375 nm (free running). The laser beams for both internal and external production are the same (photoionization lasers in Fig. 1). The laser for the degenerate $^1S_0 \rightarrow ^1P_1$ transition (423 nm) has to be tuned differently for the production inside the Paul trap ($B = 0$ tesla) and inside the Penning trap ($B = 7$ tesla). For the latter, the nondegenerate transition $^1S_0 \rightarrow ^1P_{1,+1}$ is chosen.

Figure 2(a) shows the electrostatic potential and magnetic field along the beam line in the axial direction. The Paul trap [30] is operated for these experiments at a radio frequency $\omega_{RF} = 2\pi \times 600$ kHz with $V_{RF} = 230$ V_{pp}. This corresponds to q_z and q_r values of ≈ 0.49 and 0.25, respectively. In the extraction process, the RF field is switched off with a decay time constant of the order of a microsecond, and one of the outer rings in the Paul trap (SE in Fig. 1) is pulsed, providing the dc potential shape in the axial direction to push the ions towards the Penning trap. The RF phase is not locked during the extraction. The measured ions' kinetic energy is centered at 150.8(7) eV [horizontal dashed line in Fig. 2(b)], with a standard deviation of 10.4 eV. A movable microchannel plate (MCP) detector is located at the end of the beam line for diagnosis. The mean time-of-flight of the $^{40}\text{Ca}^+$ ions from the Paul trap to the MCP detector at the end of the beam line is 83.9 μs with $\Delta t_{FWHM} = 5.5$ μs . The time-of-flight from the

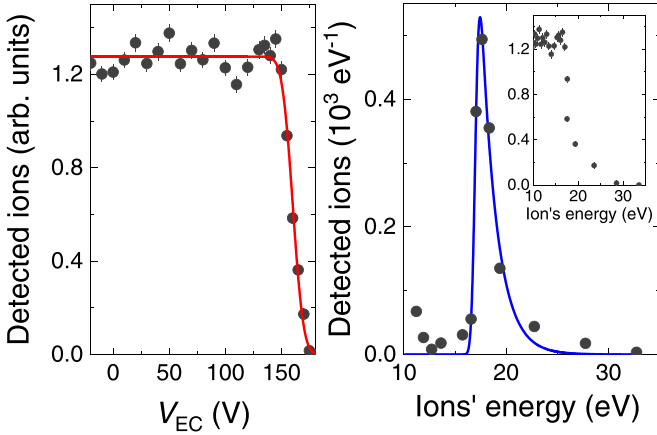


FIG. 4. Energy spread of the ions in the Penning trap before cooling. The data points in the left panel are the number of detected ions with time-of-flight between 30 and 60 μs for different values of V_{EC} [some of them are shown in Fig. 2(c)]. The right panel shows the data points from the derivative of the number of detected ions as a function of the trapped ion's energy, shown in the inset. The blue-solid line is the fit using an exponentially modified Gaussian distribution.

Paul trap to the Penning trap is centered at 47 μs . The voltage configurations for injection and trapping in the open-ring Penning trap are depicted in Fig. 2(b). The trapping efficiency is $\approx 30\%$. It is obtained from the ratio between the detected ions ejected from the Penning trap and the detected ions in transmission. The voltages applied for trapping are $V_{\text{EC}} = 180\text{ V}$, $V_{\text{CE}} = 168\text{ V}$, and $V_{\text{RE}} = 150\text{ V}$. The ions are extracted from the open-ring Penning trap under different configurations, i.e., by applying different voltages to the endcap electrode V_{EC} . Some of these voltages are shown in Fig. 2(c). Figure 3 shows time-of-flight distributions for the configurations marked from (i) to (vi) in Fig. 2(c). These measurements serve to obtain the energy spread of the trapped ions. The left panel of Fig. 4 shows the number of detected ions versus V_{EC} . This number does not increase when the potential barrier decreases from a certain level. Only when the trap is fully open [dash-dotted red line in Fig. 2(c)], the count rate increases by 14(2)% due to low-energy ions. The number of detected ions is shown as a function of the trapped ions' energy in the inset of the right panel after considering the simulation results in Fig. 2(c). The right panel is obtained from the derivative of the data in the inset. An exponentially modified Gaussian distribution is used for the fit. $E = 17.0(1)\text{ eV}$ with a standard deviation of 1.5 eV is obtained for the trapped ions.

The transitions for Doppler cooling in 7 tesla are shown in Fig. 5, following the scheme presented in Ref. [26]. In that publication, only cooling in the axial direction was applied (solid arrows in Fig. 5). Radial cooling [36] (dashed arrows) was introduced later and applied with and without axialization for the experiments presented here (for axialization, see, e.g., [7]). The laser system comprises one free-running diode laser ($\lambda = 375\text{ nm}$) and 10 tunable diode lasers emitting at $\lambda = 397\text{ nm}$ (B1, B2, and B3), $\lambda = 866\text{ nm}$ (R1, R2, R3, and R4), $\lambda = 854\text{ nm}$ (R5 and R6), and $\lambda = 423\text{ nm}$, stabilized by means of two wavelength meters (WSU and WS8 from HIGH-FINESSE [37]), as shown in Fig. 5, both with absolute

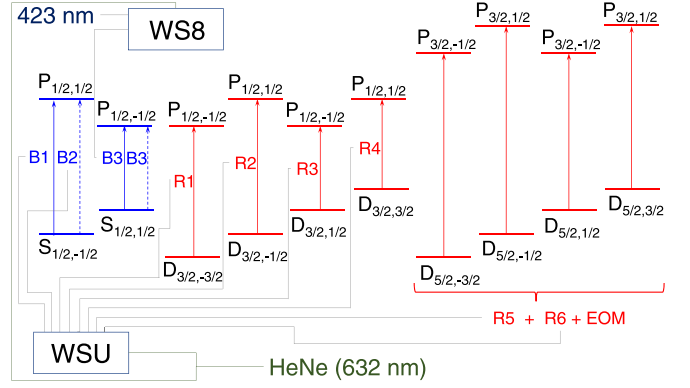


FIG. 5. Driven transitions in the $^{40}\text{Ca}^+$ ion to perform Doppler cooling in 7 tesla [26]. Two wave meters are used to regulate the nine laser frequencies needed in the experiment for cooling (B1–B3) and pumping the dark states (R1–R6), and the 423-nm laser for photoionization. See text for further details.

accuracies of 10 MHz and calibrated by means of a HeNe laser every 180 seconds. The standard deviation of the laser frequencies while running the experiment is in the range 400–700 kHz for B1, B2, and B3. The laser powers have been varied in the different measurements. For the single ion and two-ion crystal, these were about 520 μW (B1), 340 μW (B2), 280 μW (B3_{axial}), and 1.6 mW (B3_{radial}). The laser powers for R1–R6 range from 380 μW to 1.75 mW. We define the beam diameter as the distance from I_{max} down to I_{max}/e^2 in the beam profile monitor. For the cooling-laser beams in the radial direction, the diameters are measured externally at distances from the laser outputs equal to the distances to the trap center resulting in 320 μm (B2) and 220 μm (B3). In the axial direction, the values amount to 500 μm for B1 and B3 and about 1.6 mm for the IR lasers. The experiment is running with all laser beams above saturation. An estimation of the ion's temperature has been obtained from plasma considerations in large crystals (see the Appendix).

III. PENNING-TRAP RESULTS: SINGLE ION AND TWO-ION CRYSTALS

The motion of a single ion with mass m and electronic charge q in a Penning trap with a magnetic field $\vec{B} = B\vec{k}$ is the superposition of three eigenmotions [38], one in the axial direction defined by the unitary vector \vec{k} , with characteristic frequency ω_z independent of the magnetic field, and two in the radial plane with frequencies ω_c' and ω_m , fulfilling the relationship

$$\omega_c'^2 + \omega_z^2 + \omega_m^2 = \omega_c^2, \quad (1)$$

where

$$\omega_c = \frac{qB}{m} \quad (2)$$

is the cyclotron frequency. $\omega_c' = \omega_c/2 + \omega_1$ and $\omega_m = \omega_c/2 - \omega_1$, with

$$\omega_1 = \frac{\sqrt{\omega_c^2 - 2\omega_z^2}}{2}. \quad (3)$$

For more than one trapped ion besides the center-of-mass motion, other motional modes also play a role. Two identical ions in a Penning trap are cooled with lasers until they form a crystalline structure. In our experiment, the orientation of the crystal along the magnetic field is energetically favorable. For this configuration, the mode frequencies in the radial plane are given by [15]

$$\Omega_{c',m}^{\pm} = \frac{\omega_c}{2} \left[1 \pm \sqrt{1 - 2 \left(\frac{\Omega_z^{\pm}}{\omega_c} \right)^2} \right], \quad (4)$$

where

$$\Omega_z^- = \omega_z, \quad \Omega_z^+ = \sqrt{3}\omega_z \quad (5)$$

are the eigenfrequencies in the axial direction. One can define as well

$$\omega_1^{\pm} = \frac{\sqrt{\omega_c^2 - 2(\Omega_z^{\pm})^2}}{2}. \quad (6)$$

The quantum Hamiltonian of the crystal, up to the ground-state energy, can be written in terms of creation and annihilation operators [8],

$$\begin{aligned} H = & \hbar\Omega_z^+ a_+^\dagger a_+ + \hbar\Omega_z^- a_-^\dagger a_- \\ & + \hbar\Omega_{c'}^+ b_{c',+}^\dagger b_{c',+} + \hbar\Omega_{c'}^- b_{c',-}^\dagger b_{c',-} \\ & - \hbar\Omega_m^+ b_{m,+}^\dagger b_{m,+} - \hbar\Omega_m^- b_{m,-}^\dagger b_{m,-}, \end{aligned} \quad (7)$$

with the annihilation operator of the axial modes,

$$a_{\pm} = \frac{1}{\sqrt{2\hbar}} \left(\sqrt{m_s \Omega_z^{\pm}} z_{\pm} + i \sqrt{\frac{1}{m_s \Omega_z^{\pm}}} p_{z,\pm} \right), \quad (8)$$

and the annihilation operators of the radial modes: modified-cyclotron normal modes $b_{c',+}$, $b_{c',-}$ and magnetron normal modes $b_{m,+}$, $b_{m,-}$ given by

$$b_{k,\pm} = \frac{1}{\sqrt{2\hbar}} \left(\sqrt{\frac{m\omega_1^{\pm}}{2}} k_{\pm} + i \sqrt{\frac{2}{m\omega_1^{\pm}}} p_{k,\pm} \right). \quad (9)$$

The minus sign in the last two terms in Eq. (7) establishes the instability of the magnetron modes which needs to be overcome in the cooling process.

A. Cooling of externally produced ions

External ion production has improved the vacuum conditions in the Penning trap. It is also mandatory in order to implement an unbalanced crystal [15] and to perform motional quantum metrology in a Penning trap [8] or other laser-based experiments (see, e.g., [26]). Figure 6 shows single laser-cooled ions and balanced ion crystals when $V_{EC} = 180$ V, $V_{CE} = 168$ V, and $V_{RE} = 150$ V, corresponding to a measured value of $\omega_z = \Omega_z^- = 2\pi \times 333$ kHz. The images are collected with an electron-multiplying charge-coupled-device (EMCCD) camera and are the average of 10 acquisitions each with a time window of one second. The magnification of the optical system is around $18\times$ and is corrected for aberrations. The radial laser beams are directed perpendicular to the magnetic field (z) axis in Fig. 6. Radial

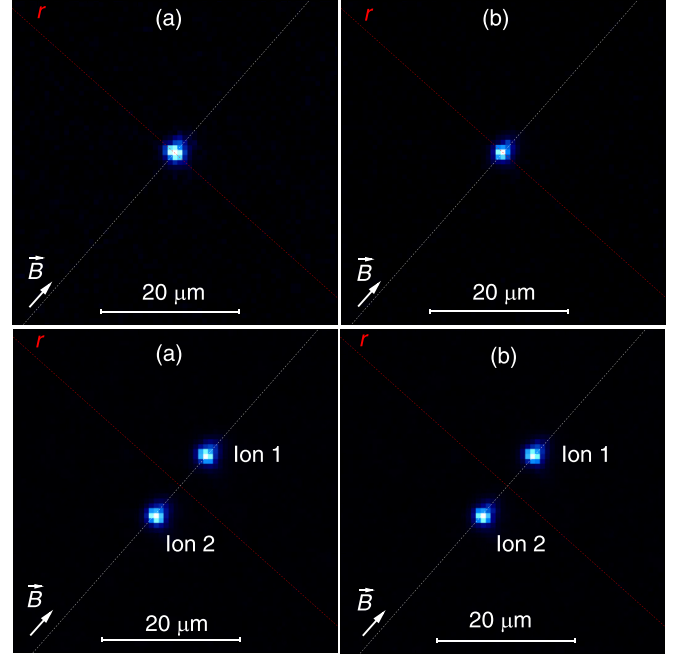


FIG. 6. Single $^{40}\text{Ca}^+$ ion and balanced crystal in the open-ring Penning trap when the ions are created in the Paul trap, extracted, transferred, captured, and laser cooled in the Penning trap. Axialization is applied in (b). See text for further details.

cooling is accomplished for both the single ion and the two-ion crystal, displacing the radial beams with respect to the trap center along the r line [Fig. 6(a)], and combining this with the application of a quadrupolar radio-frequency (RF) field at $\omega_c = 2\pi \times 2.689\,370$ MHz [Fig. 6(b)] to exchange energy between the radial motions or modes, with amplitudes of 100 and 25 mV_{pp} for the single ion and the two-ion crystal, respectively.

The EMCCD image provides more sensitive information of the system after Doppler cooling, compared to measuring the number of photons with a photomultiplier tube (PMT). For example, the projections in the radial direction of the images in the upper panel of Fig. 6 yield (a) $\Delta r_{\text{FWHM}} = 2.25(17)$ μm and (b) $\Delta r_{\text{FWHM}} = 1.87(9)$ μm , respectively, while with the PMT one cannot observe differences in the number of photons. However, the time for cooling can be better monitored with the PMT. Figure 7 shows the photons signal-to-noise ratio for a single laser-cooled $^{40}\text{Ca}^+$ ion recorded with a PMT simultaneously with the image in the EMCCD camera. Using the PMT, it is possible to utilize acquisition windows as short as 500 μs .

We have investigated the time t needed to cool a single $^{40}\text{Ca}^+$ ion and to form a $^{40}\text{Ca}^+ - ^{40}\text{Ca}^+$ crystal when these are injected externally. Under perfect vacuum, this time t can be estimated using the model described in Ref. [39]. Defining $s = I/I_s$ as the saturation parameter and $E_0 = \hbar\Gamma\sqrt{1+s/2}$ with $\Gamma = \Gamma(^{40}\text{Ca}^+) = 2\pi \times 21.6$ MHz ($S_{1/2} \rightarrow P_{1/2}$ transition), t is related to the initial trapped ion's energy E by

$$t = \frac{4}{3} t_0 \sqrt{r} \left(\frac{E}{E_0} \right)^{3/2}, \quad (10)$$

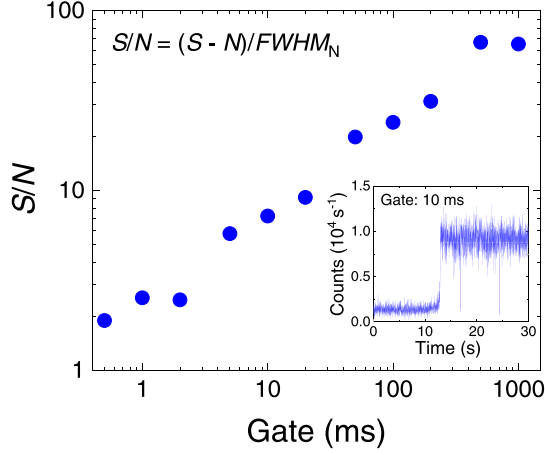


FIG. 7. 397-nm photons signal-to-noise ratio from a single laser-cooled $^{40}\text{Ca}^+$ ion in the open-ring Penning trap as a function of the acquisition gate in the photomultiplier tube. The inset shows the PMT signal for a time window of 30 s and a gate of 10 ms. The FWHM_N is obtained from the standard deviation of the background signal.

with $t_0 = (1 + s)/(s\Gamma/2)$ and $r = (\hbar K)^2/(2mE_0)$, with K the photon's wave number. In a series of 17 measurements with a single ion, we obtain $t = 165(64)$ seconds. We assume that the main energy is in the axial motion as inferred from the measurements in Sec. II.

Taking $s = 3.8$, it is possible to deduce a lower limit for E of 4.2(2.3) eV, which does not coincide with the value obtained in Sec. II, for the main ion distribution. We can attribute the energy difference to the interaction between the ions and the residual-gas atoms. To prove this, we do not switch on laser cooling until a time t_B after ion injection. The subsequent time needed for the ion to be laser cooled to the Doppler limit was shorter for longer times t_B . For a total of 16 measurements with t_B ranging from 0 to 200 s, we can extract a decay-time constant of 225 s, which only depends on collisions between the ions and the gas atoms, and therefore is applicable to any ion species. The cooling time for an unbalanced crystal will thus be shorter in the presence of residual-gas atoms and appropriate for the experiments envisaged since the trapping time is above one hour.

B. The two-ion crystal in a high magnetic field

By tuning the trap, we have covered a frequency range of $\Omega_z^-/2\pi = 170\text{--}504$ kHz. Figure 8 shows the axial-frequency values for different potentials applied to the trap electrodes. It also indicates the ion-ion distances from calculations including the uncertainties from the projection (Gaussian distributions) of the EMCCD image in the axial direction. Table I shows the frequency values of the motional modes for the $^{40}\text{Ca}^+ - ^{40}\text{Ca}^+$ crystals built in this work, corresponding to the same data points appearing in Fig. 8. The large strength of the magnetic field allows us to reach large values of Ω_z^\pm , maintaining very large Ω_z^\pm . The main issue to be overcome after Doppler cooling is the magnetron motion with large $\langle n_m \rangle$, where n represents the phonon number. Larger values of $\omega_{c'}$ and ω_m due to the high magnetic field imply lower $\langle n_{c'}$

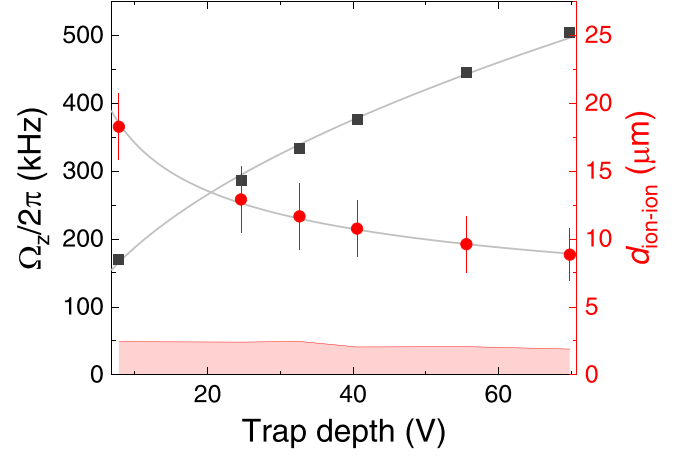


FIG. 8. Evolution of the common axial frequency measured (solid squares) and optically determined ion-ion distance (solid circles) vs trap depth. The solid lines are fits to the data points. The fitting function for the frequency data is proportional to the square root of the trap depth, while that for $d_{\text{ion-ion}}$ is inversely proportional to the cube root. The values of the axial frequencies are listed in the third column in Table I. The uncertainties of the calculated ion-ion distance represent 2σ of the projection from the photon distribution of a single ion. In this representation, one of the ions in the crystal is at zero and the red-shaded area displays the 2σ range.

and $\langle n_m \rangle$, further reducing $\langle n_m \rangle$ when applying axialization [7].

The large magnetic field also improves the efficiency of axialization. The introduction of a quadrupolar RF driving field $A(t)$ in the radial plane generally has the Hamiltonian form

$$H_{\text{ax}} = A(t) \sum_{j=1,2} (x_j^2 - y_j^2), \quad (11)$$

where $A(t)$ is in units of energy per area, and the index j refers to each of the ions. This term is invariant under the normal mode transformation of $u_\pm = (u_1 \pm u_2)/\sqrt{2}$ with $u = x, y$,

TABLE I. Motional modes frequencies of a $^{40}\text{Ca}^+ - ^{40}\text{Ca}^+$ crystal for different trap depths in a magnetic field of 7 tesla. The common axial frequencies have been probed using an external dipolar field in the axial direction. They are plotted for the different trap configurations in Fig. 8. The radial frequencies are calculated using Eq. (4) and the stretch axial frequency using Eq. (5). V_{TD} represents the trap depth in volts.

$\Omega_z^-/2\pi$ (MHz)	$\Omega_z^+/2\pi$ (MHz)	$\Omega_z^-/2\pi$ (kHz)	$\Omega_z^+/2\pi$ (kHz)	$\Omega_m^-/2\pi$ (kHz)	$\Omega_m^+/2\pi$ (kHz)	V_{TD} (V)
2.684	2.673	170	294	5.4	16	7.8
2.674	2.643	286	495	15	46	24.6
2.669	2.626	333	577	21	63	32.6
2.663	2.608	376	651	27	81	40.6
2.652	2.574	445	771	37	115	55.6
2.641	2.539	504	873	48	150	69.8

yielding

$$H_{\text{ax}} = A(t) \sum_{j=\pm} (x_j^2 - y_j^2). \quad (12)$$

Further, after expressing this in terms of creation and annihilation operators and transforming into modified-cyclotron and magnetron modes, we obtain

$$H_{\text{ax}} = A(t) \sum_{j=\pm} 2X_j^2 (ib_{c',j} b_{m,j}^\dagger + \text{H.c.}) + A(t) \sum_{j=\pm} X_j^2 (b_{c',j}^2 + b_{c',j}^{\dagger 2} - b_{m,j}^2 - b_{m,j}^{\dagger 2}), \quad (13)$$

where $X_j = \sqrt{2\hbar/(m\omega_j^\pm)}$, with ω_j^\pm defined in Eq. (6) and $b_{k,\pm}$ in Eq. (9).

A driving of the form $A(t) = A_{\text{ax}} \sin(\omega_c t)$ allows for the introduction of a rotating wave approximation (RWA) in the interaction picture with respect to H , and thus

$$H'_{\text{ax}} = A_{\text{ax}} \sum_{j=\pm} X_j^2 (ib_{c',j} b_{m,j}^\dagger + \text{H.c.}), \quad (14)$$

which increases its validity with increasing magnetic field B . This term corresponds to a phonon exchange between magnetron and modified-cyclotron modes. As shown below, this is the reason why both modes end up sharing the same amount of phonons after axialization. Due to the smaller frequency, this means the magnetron motion will end up with a much smaller temperature than the modified-cyclotron motion. For axialization, we start considering the modified-cyclotron and magnetron motion of a single ion. The effect of cooling may be expressed in terms of the following master equation in the interaction picture with respect to Eq. (7):

$$\begin{aligned} \dot{\rho} = & -iA_{\text{ax}}X^2[(ib_{c'}b_m^\dagger + \text{H.c.}), \rho] \\ & + \sum_{j=c',m} R_j^h \left(b_j^\dagger \rho b_j - \frac{1}{2} b_j b_j^\dagger \rho - \frac{1}{2} \rho b_j b_j^\dagger \right) \\ & + \sum_{j=c',m} R_j^c \left(b_j \rho b_j^\dagger - \frac{1}{2} b_j^\dagger b_j \rho - \frac{1}{2} \rho b_j^\dagger b_j \right), \end{aligned} \quad (15)$$

where R_j^c and R_j^h represent the cooling and heating rate of the corresponding mode, respectively. These rates correspond, respectively, to the absorption and emission strengths of the optical transition at the detuning of the mode's frequency [40]. Without axialization ($A_{\text{ax}} = 0$), each motion cools at a constant rate $R_j = R_j^c - R_j^h$ and reaches a final phonon number $\langle n_j \rangle_f = R_j^h/R_j$. With axialization, assuming the cooling rates are still constant, the dynamics are described by the equations

$$\begin{aligned} \frac{d}{dt} \langle n_{c'} \rangle &= -A_{\text{ax}}X^2 \langle c \rangle - R_{c'} \langle n_{c'} \rangle + R_{c'}^h, \\ \frac{d}{dt} \langle n_m \rangle &= A_{\text{ax}}X^2 \langle c \rangle - R_m \langle n_m \rangle + R_m^h, \\ \frac{d}{dt} \langle c \rangle &= -\frac{R_{c'} + R_m}{2} \langle c \rangle + 2A_{\text{ax}}X^2 (\langle n_{c'} \rangle - \langle n_m \rangle), \end{aligned} \quad (16)$$

where $c = b_{c'} b_m^\dagger + b_{c'}^\dagger b_m$. This term works towards reducing the phonon difference between both motions. The steady-state occupation under axialization then becomes

$$\langle n_{c'} \rangle_f^{\text{ax}} = \frac{4A_{\text{ax}}^2 X^4 \langle n_{\text{ax}} \rangle + R_{c'} R_m \langle n_{c'} \rangle_f}{4A_{\text{ax}}^2 X^4 + R_{c'} R_m}, \quad (17)$$

$$\langle n_m \rangle_f^{\text{ax}} = \frac{4A_{\text{ax}}^2 X^4 \langle n_{\text{ax}} \rangle + R_{c'} R_m \langle n_m \rangle_f}{4A_{\text{ax}}^2 X^4 + R_{c'} R_m}, \quad (18)$$

where we have defined

$$\langle n_{\text{ax}} \rangle = \frac{R_{c'} \langle n_{c'} \rangle_f + R_m \langle n_m \rangle_f}{R_{c'} + R_m}, \quad (19)$$

which is the phonon number both motions end up sharing under strong axialization $A_{\text{ax}}X^2 \gg \sqrt{R_{c'} R_m}/2$:

$$\langle n_{c'} \rangle_f^{\text{ax}} = \langle n_m \rangle_f^{\text{ax}} = \langle n_{\text{ax}} \rangle. \quad (20)$$

This holds true provided R_j^c and R_j^h are constant [40]. This might not be the case when A_{ax} is too large [41]. Under the best conditions observed while tuning the radial laser beams, the improvement introduced by applying axialization has been clearly observed from the projections of images as those shown in Fig. 6, along the radial direction. We have analyzed a set of subsequent measurements and the mean values of the FWHM from the single-ion projections in the radial direction are $\langle \text{FWHM} \rangle = 2.25(17) \mu\text{m}$ when axialization is not applied, and $\langle \text{FWHM}^{\text{ax}} \rangle = 1.87(9) \mu\text{m}$ when $V_{\text{ax}} = 100 \text{ mV}_{\text{pp}}$. Note that $A_{\text{ax}} \propto V_{\text{ax}}$ and V_{ax} is the amplitude of the quadrupolar field applied (V_{pp}). The uncertainties correspond to one standard deviation. The position of the ion along the radial direction does not change [$\Delta r = 10(80) \text{ nm}$]. This shows a significant improvement when applying axialization. The values of V_{ax} optimal for the single-ion case are in the range 50–150 mV_{pp} , observing for $V_{\text{ax}} = 150\text{--}250 \text{ mV}_{\text{pp}}$ a slightly worse performance increasing with V_{ax} , although still better compared to the case where $V_{\text{ax}} = 0 \text{ mV}_{\text{pp}}$, as shown in Fig. 9. This behavior does not follow the ideal case of Eq. (20), where R_j^c and R_j^h were kept constant and unaffected by the strength of A_{ax} . The FWHM in the axial direction remains the same from $V_{\text{ax}} = 0$ to $V_{\text{ax}} = 250 \text{ mV}_{\text{pp}}$.

Axialization of the common and breathing mode of the crystal in the radial plane should be accomplished with the same RF of the field since $\Omega_{c'}^\pm + \Omega_m^\pm \approx \omega_c$ (Table I). In this respect, the common radial modes can be treated similarly to the radial motions of a single ion [Eq. (16)]. However, this might not be the case for the breathing modes, which, although following the same equation, are expected to differ in the cooling rates.

The values of the FWHM from the projections in the radial directions of the images of the two ions in Fig. 6 are $\langle \text{FWHM} \rangle = 2.40(14) \mu\text{m}$ and $\langle \text{FWHM}^{\text{ax}} \rangle = 2.09(16) \mu\text{m}$ for ion 1, and $\langle \text{FWHM} \rangle = 2.36(16) \mu\text{m}$ and $\langle \text{FWHM}^{\text{ax}} \rangle = 2.01(17) \mu\text{m}$ for ion 2. For this measurement, $V_{\text{ax}} = 25 \text{ mV}_{\text{pp}}$. For larger values of V_{ax} , the two ions align on the radial plane, as shown for two cases in Fig. 9. The crystal becomes stable again for $V_{\text{ax}} \geq 425 \text{ mV}_{\text{pp}}$. In this region (III) in Fig. 9, the position of the ion crystal moves by about 1 $\text{nm}/\text{mV}_{\text{pp}}$. This might be due to deviations from the ideal quadrupolar field arising from mechanical imperfections or small misalignments between electrodes. This hypothesis is

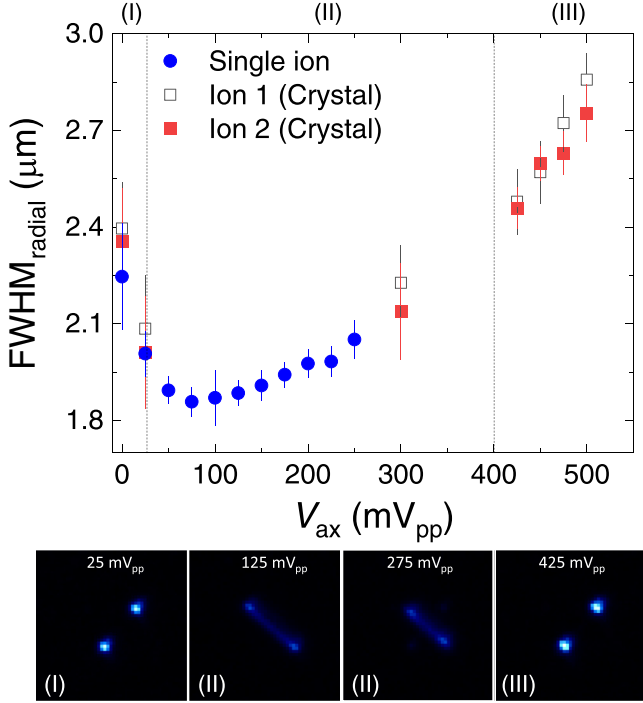


FIG. 9. Evolution of the $(\text{FWHM})_{\text{radial}}$ as a function of the axialization amplitude for one ion and for the two ions forming a balanced crystal. The crystal is stable along the axial direction in regions (I) and (III). Each data point is the average of 10 consecutive measurements. In region (II), the crystal is oriented most of the time in the radial plane. In this particular series of measurements, for $V_{\text{ax}} = 300 \text{ mV}_{\text{pp}}$, the crystal is oriented along the axial direction most of the time. Some characteristic images from the different regions are shown.

reinforced by observing the increasing trend in $(\text{FWHM})_{\text{radial}}$ in Fig. 9.

While for a single ion these possible effects do not counteract the improvement due to axialization when $V_{\text{ax}} > 25 \text{ mV}_{\text{pp}}$, this is not the case for two ions [region (II) in Fig. 9]. Although $\Omega_{c'}^{\pm} + \Omega_m^{\pm} \approx \omega_c$, the two-ion crystal along the magnetic field axis can be perturbed more easily, as observed in Fig. 9, and thus the crystalline structure will be more sensitive to possible deviations from the ideal quadrupolar field. Our theoretical approach is based on a harmonic approximation around the axial potential minima of each ion. This approximation is valid as long as the axial angular momentum L_z of the crystal remains negligible. Beyond a certain threshold of L_z , the potential minima align on the radial plane instead, rendering the axial configuration unstable and the radial one stable. Due to their axial symmetry, the bare Penning-trap potentials conserve L_z and cooling contributes to its reduction. Therefore, the axial configuration is stable for most cooling scenarios. Nevertheless, this is not necessarily the case in the presence of axialization. Axialization breaks the axial symmetry and therefore has the potential to increase L_z . The breathing mode, being the only one affected by the nonlinear Coulomb repulsion, is most susceptible to this effect. Together with the possibility of small misalignments mentioned above, this intriguing behavior is the result

of nonlinear effects that establish the ground for further investigation.

IV. CONCLUSIONS AND OUTLOOK

In this paper, we have shown a single laser-cooled ion and a two-ion crystal in a 7-tesla Penning trap when the ion species ($^{40}\text{Ca}^+$) is produced by photoionization in a Paul trap in the absence of a magnetic field, extracted, transported, and captured in-flight in the open-ring Penning trap. Balanced crystals have been formed for several trap configurations, allowing a range of common axial frequencies of a few-hundred kHz. The energy of the ions with respect to the minimum of the trap potential is a few electronvolts. The effect of having a high-magnetic-field strength has also been analyzed and we have found two advantages. First, the high magnetic field reduces the contribution of residual terms counteracting the cooling process of the radial motion under axialization. Second, the same field will yield a smaller mean phonon number in the magnetron motion in the axialization process if the cooling rate of the modified-cyclotron motion (single ion) or modes (two-ion crystal) is much larger than the magnetron ones. Although the advantage of axialization has been demonstrated for a single laser-cooled ion, the results are not optimal for the balanced crystal, which is more sensitive to perturbations, for example, arising from misalignments of the electrodes and with cooling rates for the common (such as the single-ion case) and stretch modes that can be different. In order to achieve similar cooling results for both modes, different optimal amplitudes (V_{ax}) should be applied for each. This is not possible since both modes require the same axialization frequency ω_c . This problem will be lifted in the case of unbalanced crystals since the relationship $\Omega_{c'}^{\pm} + \Omega_m^{\pm} \approx \omega_c$ does not hold.

The performance of the system, obtained from the fluorescence images, suggests that Doppler cooling of an unbalanced crystal made of a $^{40}\text{Ca}^+$ ion and any other charged particle is feasible, overcoming the instability of the magnetron motion and allowing one to use the platform for motional metrology or other laser-based or laser-assisted experiments. Motional metrology has been presented proposing $^{232}\text{Th}^+$ as the target ion [8]. The production and injection of this ion species is currently under investigation. When $\omega_z/2\pi = 333 \text{ kHz}$, the frequencies of the motional modes of the crystal $^{232}\text{Th}^+ - ^{40}\text{Ca}^+$ using the linear approximation [15], which is valid in the quantum regime, are $\Omega_{c'}^-/2\pi = 2.647 \text{ MHz}$, $\Omega_{c'}^+/2\pi = 416 \text{ kHz}$, $\Omega_m^-/2\pi = 68 \text{ kHz}$, $\Omega_m^+/2\pi = 21 \text{ kHz}$, $\Omega_z^-/2\pi = 165 \text{ kHz}$, and $\Omega_z^+/2\pi = 482 \text{ kHz}$. This requires two quadrupolar fields for axialization, i.e., one at a frequency $\Omega_{c'}^- + \Omega_m^- \approx 2\pi \times 2.715 \text{ MHz}$ and another with $\Omega_{c'}^+ + \Omega_m^+ \approx 2\pi \times 437 \text{ kHz}$. This will allow one to apply two quadrupolar fields simultaneously and observing the cooling of the two modes. In any case, in order to measure the final temperature and to carry out experiments of quantum metrology with the unbalanced crystal, the $S_{1/2} \rightarrow D_{5/2}$ (clock) transition in $^{40}\text{Ca}^+$ [42] needs to be addressed to bring the crystal into the ground state and to accurately measure the motional frequencies of its common and breathing modes.

ACKNOWLEDGMENTS

We acknowledge support from the Spanish MICINN through Project No. PID2019-104093GB-I00/AEI/10.013 39/501100011033 and Contract No. PTA2018-016573-I, from the Andalusian Government through Project No. P18-FR-3432 and Fondo Operativo FEDER A-FQM-425-UGR18, from the Spanish Ministry of Education through PhD fellowship No. FPU17/02596, and from the University of Granada “Plan Propio - Programa de Intensificación de la Investigación,” Project No. PP2017-PRII-04, and “Laboratorios Singulares 2020.” The construction of the facility was supported by the European Research Council (Contract No. 278648-TRAPSENSOR), Projects No. FPA2015-67694-P and No. FPA2012-32076, infrastructure Projects No. UNGR10-1E-501, No. UNGR13-1E-1830, and No. EQC2018-005130-P (MICINN/FEDER/UGR), and Grants No. IE-5713 and No. IE2017-5513 (Junta de Andalucía-FEDER). J.C. acknowledges support from the Spanish MICINN (“Beatriz Galindo”

Fellowship No. BEAGAL18/00078). C.O. acknowledges funding through DFG from SFB / CRC 1227 DQ-mat.

APPENDIX: IONS’ TEMPERATURE IN THE COULOMB CRYSTAL

Here we show ion Coulomb crystals (ICCs) and we use one of them to extract the ions’ temperature. ICCs in Penning traps involving more ions have been observed and extensively studied at NIST-Boulder [32,43] (${}^9\text{Be}^+$ ions in 4.46 T) and Imperial College [33] (${}^{40}\text{Ca}^+$ ions in 1.86 T). The temperature of large [44] and small [45] ICCs has been measured with these setups using techniques beyond Doppler cooling. In the experiments reported here, ICCs have been formed as shown in Fig. 10 for ions created inside the 7-T Penning trap. The images are collected with the EMCCD camera and an acquisition time window of one second. The magnification of the optical system here is around $\times 15$.

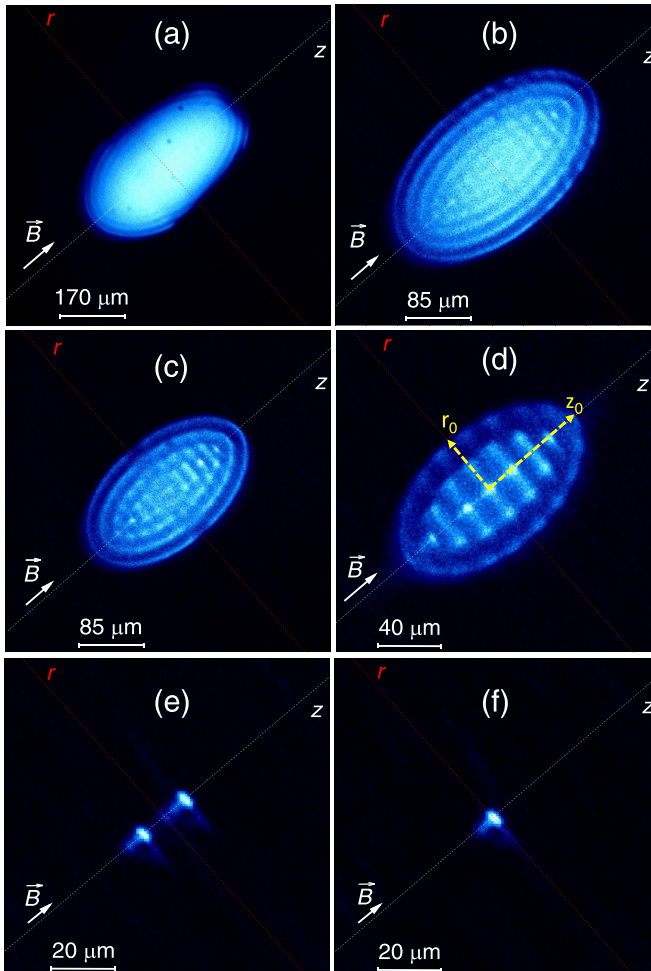


FIG. 10. Images of ICCs in the 7-tesla Penning trap formed by different amount of ions. The crystal structure becomes clearly visible from (b). In all of these cases, the ions were created inside the Penning trap. The open-ring Penning trap was operated with an axial oscillation frequency for a single ${}^{40}\text{Ca}^+$ ion in the center of the trap, $\omega_z = 2\pi \times 170$ kHz.

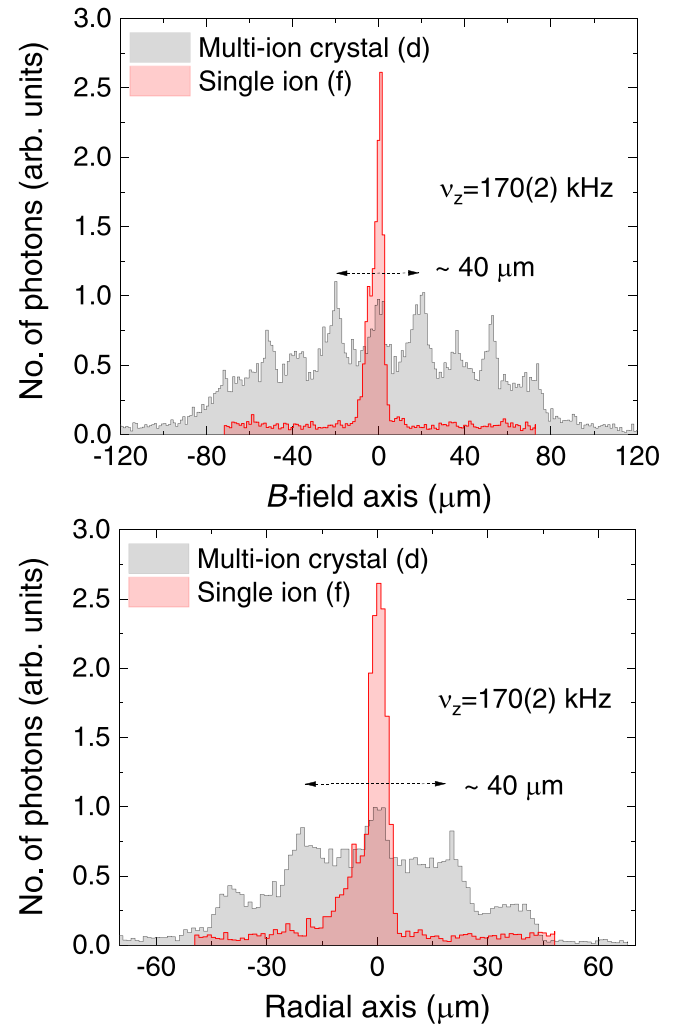


FIG. 11. Top: Projections along the magnetic field axis of the crystal shown in Fig. 10(d) and that of the single ion in Fig. 10(f). Bottom: Projections along the radial direction of the crystal shown in Fig. 10(d) and that of the single ion in Fig. 10(f). The peaks are not fully resolved in this direction due to the rotation of the crystal forming an ellipsoid around the magnetic field axis.

The crystal structure is clearly visible in Fig. 10, from Fig. 10(b) down to a single ion in Fig. 10(f). The optical system was not corrected for aberrations. Figure 11 shows the projections along the magnetic field axis and perpendicularly to it in the plane of the figure for the image in Figs. 10(d) and 10(f).

Defining the ion density n_0 , the ratio between ω_z and the plasma frequency [32],

$$\omega_p^2 = \frac{q^2 n_0}{\epsilon_0 m} = 2\omega_r(\omega_c - \omega_r), \quad (\text{A1})$$

with ϵ_0 being the vacuum permittivity and ω_r the rotation frequency of the crystal, is given as a function of the ratio $\alpha = z_0/r_0$ [Fig. 10(d)] by

$$\frac{\omega_z^2}{\omega_p^2} = \frac{1}{\alpha^2 - 1} \left[\frac{u_p}{2} \ln \left(\frac{u_p + 1}{u_p - 1} \right) - 1 \right], \quad (\text{A2})$$

with

$$u_p = \frac{\alpha}{\sqrt{\alpha^2 - 1}}. \quad (\text{A3})$$

For the case shown in Fig. 10(d), $\omega_p = 2\pi \times 386$ kHz, $\omega_r = 2\pi \times 27.8$ kHz, and $n_0 = 1.3 \times 10^8$ cm³. The ion number is ≈ 70 . From the plasma, we can estimate the temperature T observing, e.g., Fig. 11, where it is possible to extract an average ion-ion distance of ~ 20 μ m. This average distance is defined as the Wigner-Seitz radius (a_0) in the Coulomb coupling parameter [46],

$$\Gamma = \frac{e^2}{4\pi\epsilon_0 a_0 k_B T}, \quad (\text{A4})$$

where k_B is the Boltzmann's constant. Taking $\Gamma = 178$ (considering an infinite plasma) for a phase transition to occur [47], an upper limit for the temperature of $T \leq 5$ mK can be found.

-
- [1] E. A. Cornell, K. R. Boyce, D. L. K. Fyngenson, and D. E. Pritchard, *Phys. Rev. A* **45**, 3049 (1992).
- [2] S. Rainville, J. K. Thompson, and D. E. Pritchard, *Science* **303**, 334 (2004).
- [3] S. Sturm, F. Köhler, J. Zatorski, A. Wagner, Z. Harman, G. Werth, W. Quint, C. H. Keitel, and K. Blaum, *Nature (London)* **506**, 467 (2014).
- [4] S. Ulmer, C. Smorra, A. Mooser, K. Franke, H. Nagahama, G. Schneider, T. Higuchi, S. Van Gorp, K. Blaum, Y. Matsuda, W. Quint, J. Walz, and Y. Yamazaki, *Nature (London)* **524**, 196 (2015).
- [5] E. G. Myers, *Atoms* **7**, 37 (2019).
- [6] J. F. Goodwin, G. Stutter, R. C. Thompson, and D. M. Segal, *Phys. Rev. Lett.* **116**, 143002 (2016).
- [7] P. Hrmo, M. K. Joshi, V. Jarlaud, O. Corfield, and R. C. Thompson, *Phys. Rev. A* **100**, 043414 (2019).
- [8] J. Cerrillo and D. Rodríguez, *Europhys. Lett.* **134**, 38001 (2021).
- [9] P. O. Schmidt, T. Rosenband, C. Langer, W. M. Itano, J. C. Bergquist, and D. J. Wineland, *Science* **309**, 749 (2005).
- [10] D. J. Heinzen and D. J. Wineland, *Phys. Rev. A* **42**, 2977 (1990).
- [11] D. Rodríguez, *Appl. Phys. B* **107**, 1031 (2012).
- [12] J. M. Cornejo, M. J. Gutiérrez, E. Ruiz, A. Bautista-Salvador, C. Ospelkaus, S. Stahl, and D. Rodríguez, *Intl. J. Mass Spectrom.* **410**, 22 (2016).
- [13] M. Bohman, V. Grunhofer, C. Smorra, M. Wiesinger, C. Will, M. J. Borchert, J. A. Devlin, S. Erlewein, M. Fleck, S. Gavranovic, J. Harrington, B. Latacz, A. Mooser, D. Popper, E. Wursten, K. Blaum, Y. Matsuda, C. Ospelkaus, W. Quint, J. Walz *et al.*, *Nature (London)* **596**, 514 (2021).
- [14] J. M. Cornejo, R. Lehnert, M. Niemann, J. Mielke, A. Bautista-Salvador, M. Schulte, D. Nitzschke, M. J. Borchert, K. Hammerer, S. Ulmer, and C. Ospelkaus, *New J. Phys.* **23**, 073045 (2021).
- [15] M. J. Gutiérrez, J. Berrocal, F. Domínguez, I. Arrazola, M. Block, E. Solano, and D. Rodríguez, *Phys. Rev. A* **100**, 063415 (2019).
- [16] G. Gabrielse, A. Khabbaz, D. S. Hall, C. Heimann, H. Kalinowsky, and W. Jhe, *Phys. Rev. Lett.* **82**, 3198 (1999).
- [17] C. Smorra, S. Sellner, M. J. Borchert, J. A. Harrington, T. Higuchi, H. Nagahama, T. Tanaka, A. Mooser, G. Schneider, M. Bohman, K. Blaum, Y. Matsuda, C. Ospelkaus, W. Quint, J. Walz, Y. Yamazaki, and S. Ulmer, *Nature (London)* **550**, 371 (2017).
- [18] K. Blaum, J. Dilling, and W. Nörtershäuser, *Phys. Scr.* **T152**, 014017 (2013).
- [19] D. M. Lucas, A. Ramos, J. P. Home, M. J. McDonnell, S. Nakayama, J.-P. Stacey, S. C. Webster, D. N. Stacey, and A. M. Steane, *Phys. Rev. A* **69**, 012711 (2004).
- [20] M. Block, D. Ackermann, K. Blaum, C. Droese, M. Dworschak, S. Eliseev, T. Fleckenstein, E. Haettner, F. Herfurth, F. P. Heßberger, S. Hofmann, J. Ketelaer, J. Ketter, H.-J. Kluge, G. Marx, M. Mazzocco, Y. N. Novikov, W. R. Plaß, A. Popeko, S. Rahaman *et al.*, *Nature (London)* **463**, 785 (2010).
- [21] E. Minaya Ramirez, D. Ackermann, K. Blaum, M. Block, C. Droese, Ch. E. Düllmann, M. Dworschak, M. Eibach, S. Eliseev, E. Haettner, F. Herfurth, F. P. Heßberger, S. Hofmann, J. Ketelaer, G. Marx, M. Mazzocco, D. Nesterenko, Yu. N. Novikov, W. R. Plaß, D. Rodríguez *et al.*, *Science* **337**, 1207 (2012).
- [22] K. A. Gilmore, J. G. Bohnet, B. C. Sawyer, J. W. Britton, and J. J. Bollinger, *Phys. Rev. Lett.* **118**, 263602 (2017).
- [23] E. Jordan, K. A. Gilmore, A. Shankar, A. Safavi-Naini, J. G. Bohnet, M. J. Holland, and J. J. Bollinger, *Phys. Rev. Lett.* **122**, 053603 (2019).
- [24] M. Niemann, T. Meiners, J. Mielke, M. J. Borchert, J. M. Cornejo, S. Ulmer, and C. Ospelkaus, *Meas. Sci. Technol.* **31**, 035003 (2020).
- [25] C. Baker, W. Bertsche, A. Capra, C. Cesar, M. Charlton, A. C. Mathad, S. Eriksson, A. Evans, N. Evetts, S. Fabbri, J. Fajans, T. Friesen, M. Fujiwara, P. Grandemange, P. Granum, J. Hangst, M. Hayden, D. Hodgkinson, C. Isaac, M. Johnson *et al.*, *Nat. Commun.* **12**, 6139 (2021).

- [26] M. J. Gutiérrez, J. Berrocal, J. M. Cornejo, F. Domínguez, J. J. Del Pozo, I. Arrazola, J. Bañuelos, P. Escobedo, L. Lamata, R. A. Rica, S. Schmidt, M. Block, E. Solano, and D. Rodríguez, *New J. Phys.* **21**, 023023 (2019).
- [27] T. Murböck, S. Schmidt, G. Birkl, W. Nörtershäuser, R. C. Thompson, and M. Vogel, *Phys. Rev. A* **94**, 043410 (2016).
- [28] T. Leopold, S. A. King, P. Micke, A. Bautista-Salvador, J. C. Heip, C. Ospelkaus, J. C. Crespo, J. C. López-Urrutia, and P. O. Schmidt, *Rev. Sci. Instrum.* **90**, 073201 (2019).
- [29] K. Groot-Berning, F. Stopp, G. Jacob, D. Budker, R. Haas, D. Renisch, J. Runke, P. Thörle-Pospiech, C. E. Düllmann, and F. Schmidt-Kaler, *Phys. Rev. A* **99**, 023420 (2019).
- [30] J. Cornejo, M. Colombano, J. Doménech, M. Block, P. Delahaye, and D. Rodríguez, *Rev. Sci. Instrum.* **86**, 103104 (2015).
- [31] F. Domínguez, I. Arrazola, J. Doménech, J. S. Pedernales, L. Lamata, E. Solano, and D. Rodríguez, *Sci. Rep.* **7**, 8336 (2017).
- [32] J. J. Bollinger, D. J. Heinzen, F. L. Moore, W. M. Itano, D. J. Wineland, and D. H. E. Dubin, *Phys. Rev. A* **48**, 525 (1993).
- [33] S. Mavadia, J. F. Goodwin, G. Shutter, S. Bharadia, D. R. Crick, D. M. Segal, and R. C. Thompson, *Nat. Commun.* **4**, 2571 (2013).
- [34] <https://simion.com/>.
- [35] J. M. Cornejo, The preparation Penning trap and recent developments on high-performance ion detection for the project TRAPSENSOR, Ph.D. thesis, Universidad de Granada, 2016.
- [36] W. M. Itano and D. J. Wineland, *Phys. Rev. A* **25**, 35 (1982).
- [37] <https://www.highfinesse.com/>.
- [38] L. S. Brown and G. Gabrielse, *Rev. Mod. Phys.* **58**, 233 (1986).
- [39] J. H. Wesenberg, R. J. Epstein, D. Leibfried, R. B. Blakestad, J. Britton, J. P. Home, W. M. Itano, J. D. Jost, E. Knill, C. Langer, R. Ozeri, S. Seidelin, and D. J. Wineland, *Phys. Rev. A* **76**, 053416 (2007).
- [40] J. I. Cirac, R. Blatt, P. Zoller, and W. D. Phillips, *Phys. Rev. A* **46**, 2668 (1992).
- [41] N. Scharnhorst, J. Cerrillo, J. Kramer, I. D. Leroux, J. B. Wübbena, A. Retzker, and P. O. Schmidt, *Phys. Rev. A* **98**, 023424 (2018).
- [42] M. Chwalla, J. Benhelm, K. Kim, G. Kirchmair, T. Monz, M. Riebe, P. Schindler, A. S. Villar, W. Hänsel, C. F. Roos, R. Blatt, M. Abgrall, G. Santarelli, G. D. Rovera, and P. Laurent, *Phys. Rev. Lett.* **102**, 023002 (2009).
- [43] J. W. Britton, B. C. Sawyer, A. C. Keith, C. C. J. Wang, J. K. Freericks, H. Uys, M. J. Biercuk, and J. J. Bollinger, *Nature (London)* **484**, 489 (2012).
- [44] B. C. Sawyer, J. W. Britton, A. C. Keith, C.-C. Joseph Wang, J. K. Freericks, H. Uys, M. J. Biercuk, and J. J. Bollinger, *Phys. Rev. Lett.* **108**, 213003 (2012).
- [45] G. Stutter, P. Hrmo, V. Jarlaud, M. Joshi, J. Goodwin, and R. Thompson, *J. Mod. Opt.* **65**, 549 (2018).
- [46] R. C. Thompson, *Contemp. Phys.* **56**, 63 (2014).
- [47] M. D. Jones and D. M. Ceperley, *Phys. Rev. Lett.* **76**, 4572 (1996).